HHS Public Access

Author manuscript

*Int J Comput Assist Radiol Surg*. Author manuscript; available in PMC 2015 August 05.

Published in final edited form as:

*Int J Comput Assist Radiol Surg*. 2015 August ; 10(8): 1239–1252. doi:10.1007/s11548-014-1132-7.

# 2D–3D radiograph to cone-beam computed tomography (CBCT) registration for C-arm image-guided robotic surgery

**Wen Pei Liu**,
Department of Computer Science, Johns Hopkins University, Baltimore, MD, USA

**Yoshito Otake**,
Department of Computer Science, Johns Hopkins University, Baltimore, MD, USA

**Mahdi Azizian**,
Intuitive Surgical Inc., Sunnyvale, CA, USA

**Oliver J. Wagner**,
Intuitive Surgical Inc., Sunnyvale, CA, USA

**Jonathan M. Sorger**,
Intuitive Surgical Inc., Sunnyvale, CA, USA

**Mehran Armand**, and
Applied Physics Laboratory, Johns Hopkins University, Baltimore, MD, USA

**Russell H. Taylor**
Department of Computer Science, Johns Hopkins University, Baltimore, MD, USA

Wen Pei Liu: wen.p.liu@gmail.com

## Abstract

**Purpose—**C-arm radiographs are commonly used for intraoperative image guidance in surgical interventions. Fluoroscopy is a cost-effective real-time modality, although image quality can vary greatly depending on the target anatomy. Cone-beam computed tomography (CBCT) scans are sometimes available, so 2D–3D registration is needed for intra-procedural guidance. C-arm radiographs were registered to CBCT scans and used for 3D localization of peritumor fiducials during a minimally invasive thoracic intervention with a da Vinci Si robot.

**Methods—**Intensity-based 2D–3D registration of intraoperative radiographs to CBCT was performed. The feasible range of X-ray projections achievable by a C-arm positioned around a da Vinci Si surgical robot, configured for robotic wedge resection, was determined using phantom models. Experiments were conducted on synthetic phantoms and animals imaged with an OEC 9600 and a Siemens Artis zeego, representing the spectrum of different C-arm systems currently available for clinical use.

---

**Conflict of interest** Wen P. Liu, M.S. is a student fellow sponsored by Intuitive Surgical, Inc. Mahdi Azizian, Ph.D. is an employee of Intuitive Surgical, Inc. Oliver J. Wagner, M.D. is an employee of Intuitive Surgical, Inc. Jonathan M. Sorger, Ph.D. is an employee of Intuitive Surgical, Inc.

**Ethical standard** All institutional and national guidelines for the care and use of laboratory animals were followed.

**Informed Consent** Statement of informed consent was not applicable since the manuscript does not contain any patient data.

**Results—**The image guidance workflow was feasible using either an optically tracked OEC 9600 or a Siemens Artis zeego C-arm, resulting in an angular difference of $\Delta\theta$: ~ 30°. The two C-arm systems provided $TRE_{mean} \leq 2.5$ mm and $TRE_{mean} \leq 2.0$ mm, respectively (i.e., comparable to standard clinical intraoperative navigation systems).

**Conclusions—**C-arm 3D localization from dual 2D–3D registered radiographs was feasible and applicable for intraoperative image guidance during da Vinci robotic thoracic interventions using the proposed workflow. Tissue deformation and in vivo experiments are required before clinical evaluation of this system.

### Keywords

2D–3D registration; Intraoperative fluoroscopy; Robotic surgery; Image guidance

## Introduction

C-arm radiographs are commonly used for intraoperative image guidance for surgical interventions. Fluoroscopy is a real-time and cost-effective modality, although image quality can vary greatly depending on the clinical target anatomy. C-arms in clinical rotation range from older technologies, using image intensifiers, to robotic systems with motor-actuated flat-panel detectors synchronized with an X-ray source. Thus C-arm image capabilities vary from distorted single 2D planar X-ray images to 3D reconstructed volumes (i.e., cone-beam computed tomography (CBCT)).

Although radiographs provide valuable real-time projective information, for surgeons, registration of intraoperative image with respect to preoperative data can provide guidance and assessment of progress. Currently, the most utilized systems for intraoperative localization consist of optical and electromagnetic (EM) solutions, which track calibrated tools with respect to registered preoperative volumetric data. Known challenges for these systems include non-uniform accuracy throughout the volume of interest, a clear line-of-sight requirement for optical trackers and EM fields being subject to distortions by metallic equipment, ubiquitous to surgical suites. Previous assessments [1,2] of these systems in the clinical arena report accuracies ~2 mm target registration error (TRE), with higher errors within dynamic EM fields [3].

Moreover, the utilization of minimally invasive robotic-assisted surgery continues to expand, including applications in thoracic surgery. The tele-robotic approach, available with a *da Vinci* system (Intuitive Surgical Inc., Sunnyvale, CA), offers notable advantages for delicate dissection required for e.g., a systematic mediastinal or pulmonary lymphadenectomy or other intricate work in the thoracic cavity [4]. Initial results have shown promising results in regards to improved short-term outcome, when compared to open thoracotomy and even Video-Assisted Thoracoscopic Surgery (VATS) [5]. In fact, several articles show the efficacy and safety of robotic pulmonary applications including lobectomy, segmentectomy and wedge resections. Recent national [6] and multi-center [7] studies support robotic pulmonary resection as an appropriate alternative to VATS. Furthermore, preliminary results of single institutional studies on robotic lung segmentectomy [8] also support robotic intervention as a feasible and safe approach.

The major diagnostic tools to achieve adequate staging information include preoperative volumetric data (i.e., computed tomography (CT), CT angiography (CTA), positron emission tomographic (PET)–CT). The amount of lung tissue (lobe, wedge, segment) that has to be resected depends on the etiology of the tumor and, in case of malignancy, the tumor stage that describes the severity of the cancer. The tumor stage is based on the size and/or extent of the primary tumor, whether cancer cells have spread to nearby (regional) lymph nodes, and whether metastasis, the spread of the cancer to other parts of the body, has occurred. Our proposed workflow targets lung lesions ≤3 cm, indicated for wedge resection, in early-stage non-small cell lung cancer (T1). In current clinical practice, the integration of preoperative plans to the surgical scene is conducted as mental exercise; thus, the accuracy of this practice is not only a function of the surgeon's experience but subject to inconsistencies. This is further complicated by the fact that in order to create workspace for a robot-assisted surgery, the lung is collapsed with the patient rotated 90 °C laterally and overextended in the coronal plane, presenting the thoracic workspace deformed from that of preoperative image acquisitions.

However, the registration of a single fluoroscopic image with respect to preoperative CT/CBCT would present the context of live instrumentation, anatomical deformation and resection back to preoperative diagnostic volumes and the associated surgical plans. Methods and implementation for the required 2D–3D registration is an active area of research with applications not only in surgery [9,10], but also in interventional radiology and radiation therapy [11]. In fact estimation of spatiotemporal lung motion for radiotherapy has been achieved using volumetric reconstruction [12,13], 3D models [14] and single projection image [15–19]. However, these prior studies focuses on periodic respiratory lung motion, compared with our target dynamic surgical motion. Furthermore, registration from single projections is limited by ambiguities in the source-to-detector direction, i.e., depth. However, registration from two projective views can resolve localization in depth, with 3D tracking of tool positions and artificial fiducials for intraoperative navigation [20,21].

Thus, we propose providing intraoperative image guidance by tracking the tumor with a single radio-opaque metallic fiducial, placed either in diagnostic biopsy or perioperatively. In this study, we investigate the feasibility of using dual C-arm radiographs for 3D localization of the peri-tumor fiducial during a minimally invasive thoracic intervention with a *da Vinci Si* robot. Using phantom models, we determined the achievable range of X-ray projections by a C-arm positioned around a *da Vinci Si*, configured for robotic wedge resection. Experiments varied the angular differences of two fluoroscopic views acquired within the experimentally determined workspace of the C-arm-guided *da Vinci* intervention. Results show the effects of uncertainty in C-arm extrinsic and intrinsic parameters on our proposed method of 2D– 3D registration and identify their allowable range in order to achieve a desirable TRE ≤ 2 mm(i.e., comparable to current intraoperative navigation systems).

## Materials and methods

### C-arm systems

We evaluated two distinct C-arm systems from different ends of the current spectrum of technology. First, a portable C-arm fluoroscopic unit, an OEC 9600 (1998, GE OEC Medical Systems, Salt Lake City, UT), was selected to represent older technology, which uses an image intensifier (II) (tri-mode 12/9/6″). Secondly, a Siemens Artis *zeego* (*2012, Siemens Inc*.) [22], distinctly different with the integration of a flat-panel detector (30×40 cm), represents a modern, multi-articulated, robotic, digital fluoroscopy system. A detailed comparison of these two systems accounting for price and number of installations is beyond the scope of this paper; however, by assessing both types of imaging systems, we cover the spectrum of technology of C-arm systems in use today. Further experiments were conducted with the robotic C-arm system in order to highlight its more extensive capabilities as an intraoperative imaging system.

### Definitions of coordinate system

We identified a coordinate system with a patient lying headfirst supine as follows: *x* axis (medial to left), *y* axis (feet- to-head) and *z* axis (back-to-front). The projective view of a single fluoroscopic acquisition by a standard C-arm system was modeled as a pinhole camera. Using this model, a projection matrix $P \in R_{3x4}$ was used to map 3D point locations to its corresponding 2D projection in the fluoroscopic image.

$$P = K\,[R|t] \quad (1)$$

The intrinsic camera parameters were captured in $K \in R_{3x3}$, while $R \in R_{3x3}$ and $t \in R_{3x1}$ together encompassed the extrinsic camera parameters for rotation and translation, respectively. 3D point location $(X, Y, Z)^T$ were projected onto corresponding 2D image location $(u, v, 1)^T$, in a radiograph as follows

$$\begin{pmatrix} u \\ v \\ 1 \end{pmatrix} = K\,[R|t] \begin{pmatrix} X \\ Y \\ Z \\ 1 \end{pmatrix} \quad (2)$$

The intrinsic camera parameter matrix

$$K = \begin{pmatrix} SDD/p & \gamma & O_x \\ 0 & SDD/p & O_y \\ 0 & 0 & 1 \end{pmatrix} \quad (3)$$

required calibration to determine source-to-detector distance (SDD) and *p*, the pixel size were set as identical in *x* and *y* for the purposes of these experiments. Parameters $(O_x, O_y)$ represent the coordinates of the isocenter in the image plane while skew, $\gamma$, was set to zero during our analyses.

Extrinsic parameters captured the rigid transformation of the volumetric isocenter to the X-ray source. The primary rotation of a C-arm around the principal axis of a patient lying supine is indicated by the value of the left anterior oblique/right anterior oblique angle, i.e., LAO/RAO. A secondary angle (cranial/caudal, i.e., CRAN/CAUD) represents how much a C-arm has been angulated toward a patient's head (cranial) or feet (caudal). For the purposes of our experiments, the 2D fluoroscopic image acquisitions utilized were composed from projective views that varied only in LAO/RAO angles. No other extrinsic angulation was performed, including CRAN/CAUD, which remained at zero.

Extrinsic rotation $R$ can be composed as follows

$$R=R_y R_x \quad (4)$$

$$R_y=\begin{pmatrix} \cos(-\alpha) & 0 & \sin(-\alpha) \\ 0 & 1 & 0 \\ -\sin(-\alpha) & 0 & \cos(-\alpha) \end{pmatrix} R_x=\begin{pmatrix} 1 & 0 & 0 \\ 0 & 0 & -1 \\ 0 & 1 & 0 \end{pmatrix} \quad (5)$$

where $\boldsymbol{\alpha}$ = LAO/RAO and $\boldsymbol{R_x}$ (rotation of 90° around x) is a standard transformation for 2D monitor displays for radiographs. The translational part of the extrinsic parameters can be defined as

$$t=(0,0,SID)^T \quad (6)$$

where SID is the source-to-isocenter distance.

## Intraoperative C-arm-guided robotic surgery

For a fluoroscopy-guided thoracic robot-assisted surgery, we propose the usage of a C-arm with the *da Vinci* system to provide intraoperative 3D localization. Table 1 describes our proposed workflow with addition required steps, system dependent, incorporated with current clinical procedures.

A preoperative lung biopsy is performed for select cases, depending on tumor location and patient history. For patients indicated for biopsy, we would recommend the placement of a fluoroscopic-opaque fiducial (52100 Chromium 1 mm diameter spheres) during the same procedure (Step 2). Intra-operatively, if the intervention is conducted with a Siemens Artis zeego, surgeons can use the Siemens Syngo iGuide system, to place one or more fiducials, which better constrains the orientation of the tumor and boundary. Limited local deformable registration can be derived from triangulation of multiple peri-tumor fiducials. On the other hand, if an intraoperative CBCT is not available, then a preoperative CT must be registered (Step 6, right). Additionally, guidance from preoperative CT would be superior to intraoperative CBCT due to the smaller field-of-view, artifacts from-motion and additional radiation of the latter. Although both modalities have been used in lung cancer radiotherapy [23], a full comparison of the trade-offs, similar to studies conducted for head and neck applications [24,25], is beyond the scope of this work. Currently, for the purposes of work

presented, this step is accomplished by running 2D–3D registration with 1 or more radiographs until manual alignment (with respect to the preoperative volume) is achieved with respect to the preoperative volume.

Step 9 is performed as needed when 3D locations of points of interest are requested by the surgeon. We first obtain two X-rays, at different projective angles. Each X-ray is registered (2D–3D) to the preoperative CT or intraoperative CBCT. Within these dual, registered 2D projections, we locate points of interest (i.e., tool tips, peri-tumor fiducials, etc) and triangulate between the two projective views to derive their 3D location within the reconstructed patient anatomy and/or preoperative plans.

### 2D–3D registration

The 2D–3D registration algorithm we used is described in detail in [26] for applications in orthopedic spine surgery. Iteratively searching through each of the six degrees of freedom (DoF) of a rigid patient pose, the algorithm determines a transformation that best aligns synthetic projections or digitally reconstructed radiographs (DRR). DRRs are generated using forward projections of the 3D reconstructed tomograph with a parallelized ray-tracing algorithm implemented on GPUs. The 2D–3D registration optimization uses a covariance matrix adaptation evolution strategy to maximize similarity metric to estimate the transformation of the patient pose in six degrees of freedom. Termination occurred when coordinate changes became less than stopping criterion of ±0.01 (mm,°). Nominal registration parameters governing the optimizer, and C-arm geometries used in our experiments are summarized in Table 2. The initialization step added extrinsic and intrinsic perturbation (Table 3) to the ground truth positions. The optimizer step size, 5(mm,°) and lower/upper bounds ±10 (mm,°) remained constant in our experiments, while two sets of the population sizes were explored for the portable II fluoroscopy system.

The similarity of the radiograph compared with a DRR is defined in terms of gradient information (GI) [27] (Fig. 3e shows an overlay of the gradient of a registered DRR on an X-ray). The GI-based similarity metric provides a degree of robustness, with respect to inconsistent deformations between 3D and 2D data by relying upon information offered by locally rigid structures and ignoring gradients between deformed tissues. This implementation of 2D–3D registration has been shown to be robust against intraoperative foreign objects/tools, changes in patient positioning and gross anatomical deformation [28].

## Experiments

In order to determine the range of feasible intraoperative X-ray projections available during a C-arm-guided *da Vinci Si* thoracic intervention, we conducted a workspace evaluation for each system, detailed in subsection “C-arm and da Vinci Si workspace configuration.” Two phantom models, a synthetic phantom and a canine cadaver embedded with fluoroscopic-opaque targets, described in subsection “Geometric calibration and distortion correction,” were used to evaluate the workspace for the portable II and floor-mounted digital robotic fluoroscopy system, respectively. Subsection “Phantom image acquisition,” presents experimental variation of dual projection and geometric uncertainty modeled after the constraints derived from workspace configuration experiments.

### C-arm and da Vinci Si workspace configuration

An anthropomorphic chest phantom was used to determine the intraoperative workspace of the two robotic systems. For thoracic robotic surgery, the base of the patient-side-cart (PSC) of *da Vinci Si* was positioned at ~30° relative to the surgical table coincident with the target patient side (Fig. 2a). The base of the portable IIC-arm was situated orthogonally to the table, below the PSC, as shown in Fig. 2b. Alternatively, the multi-articulated robotic C-arm can approach from the head of the table and be positioned to image in the same direction (Fig. 1). In this workspace configuration, we were able to rotate the primary (LAO/RAO) angle of the C-arm of the portable II fluoroscopy system from 0° to 30° (Fig. 2b), whereas we were able to achieve (LAO/RAO) articulation from +70° to +115° (*RAO*) (Fig. 1b, c) using the floor-mounted robotic digital system. This workspace evaluation showed that a *da Vinci Si* and an OEC 9600 -/Artis zeego C-arm configured for thoracic interventions would allow intraoperative X-ray acquisitions within a scan range of ≤30° and ≤ 45°, respectively.

### Geometric calibration and distortion correction

X-ray images acquired on systems using image intensifiers (i.e., OEC 9600) exhibit several characteristic distortions due to both external and internal factors. The two main types of distortions pertinent to our experiments are tangential + radial distortion and an S-shaped sigmoidal distortion (S-distortion). Due to influence of the earth's electro-magnetic field, S-distortion is dependent on the orientation of the image intensifier. We first acquired a set of 15 images of a fluoroscopically opaque checkerboard (20×20×20 mm squares) (Fig. 3d). By modeling the X-ray system with perspective projections, we calibrated (Camera Calibration Toolbox for MATLAB®) for the intrinsics (i.e., focal lengths, optical center) of the 9600 C-arm as well as polynomial corrections for tangential + radial distortion (Fig. 3b). To rectify S-distortions, we then fitted a fifth order Bernstein polynomial to segmented corners of each calibration pose that matched *daVinci-OEC 9600* workspace projections (Fig. 3c). For extrinsic registration, we used manual segmentation from five of the ten embedded PTFE spheres in dual projections of the superflab phantom. Ground truth data for the portable II system consist of the rectified images and projection matrices composed from these intrinsic and extrinsic calibrations. We attached two grayscale printed checkerboard markers near the detector and X-ray tube, which were calibrated to a Micron tracker (Claron Technology, Toronto, ON, Canada). In contrast, X-ray images from flat-panel detectors exhibit little to no distortion, thus radiographs from the zeego were used directly, without further rectification. Intrinsic and extrinsic parameters were taken from Siemens calibration files located on the reconstruction workstation.

### Phantom image acquisition

Evaluation of each C-arm was conducted on different phantoms. For the portable II system, we attached a block of Superflab™(~50 mm × ~130 mm × ~20 mm) embedded with ten polytetrafluoroethylene (PTFE) fiducial spheres (1.6 mm diameter), to the synthetic spine of the torso phantom. Half of the fiducials were used for registration, while the other five were used for evaluation. CBCT of this phantom was acquired using Siemens syngo DynaCT, 90 kVp, 290 mA, (0.48 × 0.48 × 0.48 $mm^3$ voxel size). We then collected a series of

radiographs by rotating the portable IIC-arm from 0° to 30° while recording transformation of the optical markers attached to the source and detector.

A canine cadaver phantom was used to assess image registration with the floor-mounted robotic fluoroscopy system. To create a mock tumor target, a urethane, medium durometer spherical medical balloon (10 mm diameter), was filled with a mixture of 0.5 ml rigid polyurethane foam (FOAM-IT®) and 0.25 ml of acrylic paint. The Siemens Syngo iGuide system was used to plan the placement of the tumor and four peri-tumor metal fiducials (52100 Chromium 1 mm diameter spheres) with the lung inflated. The mock tumor was then placed in the phantom's lung, right lower lobe, using an FEP I.V. catheter (Abbocath®-T 14G × 140 mm) and confirmed with real-time fluoroscopy. Another volumetric dataset capturing the tumor and fiducials in the inflated lung was acquired using the same CBCT protocol as above.

## Dual-projection image analysis

**Portable, image intensifier (II), fluoroscopy system (OEC 9600)—**For the OEC 9600 system, the primary rotation of the arm is controlled with a passive lock mechanism indicated with visual markers drawn at 2.5° increments; therefore, we modeled the range of uncertainty in extrinsic parameters of this portable C-arm at ±3°. We estimate translational uncertainty at ±10 mm, comparable to the model for robotic system discussed below. Using the *Superflab* dataset for experiment #1 (Table 2), we added extrinsic perturbations in the range ($\Delta R$ : 3°,$\Delta T$ : 10 mm) and measured the effect of simulated systematic uncertainty on the target locations. We then registered the projection using the 2D–3D algorithm and measured the TRE for 5 target spheres (non-registration fiducials) using 20 runs (i.e., 100 fiducial point measurements). To model an alternative C-arm setup, a portable C-arm with optical tracking, we modified the range of our extrinsic uncertainty at ±2mm and ±1°, comparable to accuracies of optical trackers as reported in clinic. We repeated the same extrinsic uncertainty evaluation with perturbations in the range ($\Delta R$ : 1°, $\Delta T$ : 2 mm), experiment #2.

**Floor-mounted, multi-articulated robotic fluoroscopy system (Artis zeego)—**The canine CBCT with targets was reconstructed by a Siemens workstation using 496 fluoroscopic projections acquired in an ~180° (LAO/RAO) trajectory. Using the same projection matrices from the Siemens reconstruction, we created a set of corresponding synthetic X-rays, i.e., DRR. From these two datasets, we chose combinations of pairs of images, separated by varied angular difference in the range $\Delta\theta$: 1° – 90° and triangulated through the four peritumor fiducials to measure TRE. The display of the Siemens robotic C-arm shows rotational angles in degrees and translations in centimeters. Therefore, we modeled the range of extrinsic uncertainty, of the robotic fluoroscopy system, to be ±10 mm and ±1°. Using the *canine* dataset, we added extrinsic perturbations in the range ($\Delta R$ : 1°, $\Delta T$ : 1 – 10 mm) and measured the effect of simulated systematic uncertainty on the target locations. On both synthetic DRR (experiment #4) and robotic C-arm datasets (experiment #3) after imposing extrinsic error, we then registered the projection using the 2D–3D algorithm and measured the TRE for 25 runs (i.e., 100 fiducial point measurements). Using the *canine* dataset, we conducted additional experiments to evaluate individual rotation

versus translation effect by extending extrinsic perturbations from ($\Delta R$ : 1 – 10°, $\Delta T$ : 0 mm) and ($\Delta R$ : 0°, $\Delta T$ : 5 – 50 mm), for experiments #5 and #6, respectively. To assess robustness against intrinsic uncertainty, we conducted additional experiments to evaluate individual focal length and optical center requirements by extending intrinsic perturbations from ($\Delta F$ : 1 – 10 mm) and ($\Delta O$ : 1 – 30 *pi x*), in experiments #7 and #8, respectively.

**Accuracy evaluation—**For each dual projection, we localized $(X, Y, Z)^T_{\text{Fluoro}}$ the 3D position of each fiducial, from a single projection, derived from (2) as follows:

$$\begin{pmatrix} X \\ Y \\ Z \end{pmatrix} = \frac{1}{\lambda}(KR)^{-1} \begin{pmatrix} u \\ v \\ 1 \end{pmatrix} - (KR)^{-1} Kt \quad (7)$$

where $\lambda$ represents an arbitrary scale factor. Triangulation, using dual projections, computes the 3D intersection point by solving a least squares formulation of (7).

To determine the accuracy of the proposed workflow for intraoperative localization, we characterize the 3D registration error using a standard TRE as formulated by Fitzpatrick et al. [29], which compared 3D locations, $(X, Y, Z)^T_{\text{Fluoro}}$, from dual projections of peri-tumor fiducials to corresponding points, $(X, Y, Z)^T_{\text{CBCT}}$, in the reconstructed CBCT as follows:

$$TRE = \| T^{\text{CBCT}}_{\text{Fluoro}} \begin{pmatrix} X \\ Y \\ Z \end{pmatrix}_{\text{Fluoro}} - \begin{pmatrix} X \\ Y \\ Z \end{pmatrix}_{\text{CBCT}} \|_2 \quad (8)$$

where $T^{\text{CBCT}}_{\text{Fluoro}}$ represents the transformation determined by the 2D–3D registration which aligns 3D points from triangulation with the reconstructed CBCT.

For extrinsics registration, we used manual segmentation from five of the ten embedded PTFE spheres in dual projections of the superflab phantom. Ground truth data for the portable II system consist of the rectified images and projection matrices composed from these intrinsic and extrinsic calibrations. For the digital robotic C-arm system, static geometric calibrations of given trajectories for supported isocenters are physically calibrated to compensate for these discrepancies and the flat-panel detector provides distortion-free images. For our experiments, these projections were used as a ground truth starting point for which extrinsic perturbations were added. We projected $(X, Y, Z)^T_{\text{CBCT}}$ onto each fluoroscopic image using their given projection matrices. To assess the accuracy of these projections, we compared manual segmentation of the fiducials with their projected locations, which were found to be ≤3.3 pixels° (Fig. 4c, d).

## Results

### OEC 9600

To evaluate OEC 9600, extrinsic mean, median and max TRE for the dual projection experiments, obtained at a 30° angular separation, are summarized in Table 4. Three sets of

images were processed including the (A) original fluoroscopic images, (B) images after radial and tangential rectification and images after (C) radial, tangential and S-distortion correction. To emulate standard portable II C-arm extrinsic uncertainty perturbations of ($\Delta R$ : 3°,$\Delta T$ : 10 mm) for experiment #1 showed mean TRE at 46.0, 44.7 and 9.6 mm, for (A), (B) and (C), respectively. Perturbations of ($\Delta R$ : 1°, $\Delta T$ : 2 mm), representing an OEC 9600 with Micron Tracker in experiment #2, produced mean TREs for (A), (B) and (C) at 31.1, 26.8 and 2.4 mm, respectively.

### Artis zeego

Mean, median and max TRE for the dual projection experiments are summarized in the tables of the left column of Fig. 5. Perturbations of experiment #3 ($\Delta R$ : 1°, $\Delta T$ : 10 mm) simulated the maximum extrinsic uncertainty for the floor-mounted robotic C-arm in rotation and translation. Applying this range of error generated an initial perturbance, $TRE_{max} \leq 14$ mm, in the target angular range of $\Delta\theta$: 30° – 45°. Using 2D–3D registration, following such extrinsic perturbations, the *DRR* dataset achieved ≤ 0.5 mm for all TRE with angular differences ≥ 15° (experiment #4, boxplot in Fig. 5a). However, repeating the same experiment for the *Fluoro* radiographic images resulted in a $TRE_{mean} \leq 2.0$ mm, only for angles $\Delta\theta$: 30°–45° (box-plot in Fig. 5b).

We investigated individual effects of rotation and translation error by extending the perturbation range for isolated $\Delta R$ and $\Delta T$. Experiment #5, using the *Fluoro* dataset and introducing only rotation error as follows ($\Delta R$ : 1 – −10°, $\Delta T$ : 0 mm) with select boxplot series shown in Fig. 6. For the target angular difference range, the current 2D–3D algorithm can still achieve a $TRE_{mean} \leq 2.0$ mm for rotational disturbance ≤4°. Similarly, for translation as shown in experiment #6, boxplots of $TRE_{mean}$ from perturbations of ($\Delta R$ : 0°, $\Delta T$ : 10–35mm) are shown in Fig. 6. Overall, for the proposed robotic C-arm guidance, the current 2D–3D algorithm achieved a $TRE_{mean} \leq 2.0$ mm for translational disturbances ≤25 mm, i.e., well within the extrinsic uncertainties.

Additionally, we investigated effects of intrinsic uncertainty by perturbing $\Delta F$ *and* $\Delta O$. Using the *canine* dataset, and experiment #7 introduced focal length errors ($\Delta F$ : 1–10 mm|) with TRE results plotted in Fig. 7. The Boxplots show that in the target angular difference range, the current 2D–3D algorithm can still achieve a $TRE_{mean} \leq 2.0$ mm for focal length disturbance ≤10.0 mm. Similarly, for optical center, experiments of $TRE_{mean}$ from perturbations of ($\Delta O$ : 1 – 30 *pi x*) achieved a $TRE_{mean} \leq 2.0$ mm for optical center disturbances ≤10 pix.

## Discussion

Work presented has experimentally shown the feasibility of dual-projective radiographs to provide adequate 3D localization for minimally invasive robot-assisted lung wedge resection. Using phantom models, we determined the achievable range of X-ray projections by two different C-arm systems positioned around a *da Vinci Si*, configured for robotic thoracic intervention. For these interventions, a desirable TRE ≤ 2 mm(i.e., comparable to current intraoperative navigation systems) was achieve using the proposed method of 2D–3D registration. Nominal 2D–3D registration parameters governing the registration process

were derived from previous work including initial conditions for a robust initialization using a global search [30].

Limitations of extrinsic parameters of the C-arms and *da Vinci* workspace used in these experiments were determined with clinically relevant in vivo phantoms and workflows. Other groups have explored the potential of 3D localization using two C-arm views [20,21], including with target application in image-guided surgery [31]. However, the work presented here validates clinically relevant workspace scenarios through in vivo experiments and directly explores the feasible intraoperative configurations of two clinically available robotic systems.

2D–3D registration of X-ray image intensifier images varied greatly depending on the level of distortion correction applied. Raw X-ray images from the portable II fluoroscopy system were particularly susceptible to rotational disturbances likely due to a smaller field-of-view and lower contrast, as well as factors from distortion. While work presented requires a one-time geometric C-arm calibration for both C-arm systems, other groups have debated its necessity [32]. Calibration for S-distortion, at each possible pose, is unrealistic requirement for clinical deployment. To counter these issues, other groups have developed reliable statistical characterization of C-arm distortion from sparse calibration [33].

Throughout the experiments presented, the 2D–3D registration of a single X-ray image was completed ≤ 8(*s*), using a CUDA implementation on an NVIDIA Titan graphics card (NVIDIA, Inc., Santa Clara, CA). We expect to achieve Table 1. Step 6: 3D localization ≤ 1(min), with the following required steps completed within the indicated time:

- **a.** Acquired X-ray #1 (1 s)
- **b.** 2D–3D registration of #1 (8 s)
- **c.** Segmentation of points of interest in #1 (5 s)
- **d.** Rotate C-arm to ~45° (5 s)
- **e.** Repeat a–c for X-ray #2 (14 s)
- **f.** Triangulate points from #1 and #2 (1 s)

Although radio-opaque peri-tumor fiducials can be inserted using the iGuide system of the Siemens robotic C-arm, a fiducial placed during preoperative biopsy may be arguably simpler and more amendable to lower-cost C-arms using image intensifiers. However, our results show that with a portable II fluoroscopic C-arm a minimum mean TRE of 2.4 mm was achieved only with an optical tracker and distortion correction for each projection.

The current proposed workflow tracks a single point (i.e., peri-tumor fiducial), arguably adequate on approach for wedge resections. However, perioperative positioning for a pulmonary robotic intervention, which includes a lateral rotation and deflation of the ipsilateral lung, creates deformable changes in the workspace. To address the deformation from setup and intervention, we can modify the proposed workflow to place multiple fiducials. These additional radio-opaque points should surround the target, to adequately constrain the tracking of the orientation of the tumor. After lung deflation, a CBCT of the

patient in the lateral position can be acquired with the robotic C-arm system to capture setup changes with the fiducials in place. 2D–3D deformable registration using fluoroscopy with salient landmarks (i.e., fiducials) would require further exploration beyond the described work. Furthermore, fiducial placement near pulmonary landmarks of interest (i.e., alveolar duct (Bronchus), blood vessels (Pulmonary Artery and Vein), lymphatics and nerves) can provide guidance for segmentectomy and lobectomies.

Next steps will look into pre-clinical evaluation of the proposed workflow with robotic resections. We anticipate that Table 1. Step 6, performed under 1 min, will be adequately fast enough for an initial evaluation. Further tuning of the 2D–3D registration parameters as well as hardware upgrades and automatic segmentation software can accelerate this step even more. Other proposed requirements, added to the standard workflow (Table 1), increase intraoperative setup by 6 min + 5–15 min for each intraoperatively placed fiducial. However, the guidance provided can arguably reduce time required to locate targets of interest and delineate resection boundaries, in complicated cases.

## Conclusions and future work

Experimental results support the potential of 3D localization from dual C-arm projections for intraoperative image guidance during *da Vinci* robotic thoracic interventions. While both C-arm systems were validated with the proposed workflow, the da Vinci configuration is more streamlined with intraoperative advantages compared with the cost-effective da Vinci-OEC 9600 setup, which requires an optical tracker and distortion correction. The retrospective experiments conducted on synthetic and ex-vivo phantoms and assumption of rigid deformations are a recognized limitation of the work presented; however, future work will not only look to further validate a deployment of the image guidance system using clinically relevant in vivo experiments but also address non-rigid deformation using multi-fiducial constraints. The main goal of this study was to determine feasibility of the proposed workflow, which explored the required angular disparity between two 2D–3D registered radiographic projections in order to overcome the errors along the projection viewing direction from a single X-ray. Additional multiple projections, possibly optimized (i.e., bundle-adjustment), should continue to improve the overall accuracy and will be included in future work.

## Acknowledgments

The authors extend sincere thanks to Dr. Tao Zhao and Dr. Holger Kunze. Infrastructure support was provided from NIHR01- CA-127444, NSF EEC9731748, and the Swirnow Family Foundation. Additional support was provided by Intuitive Surgical Inc. and Johns Hopkins University internal funds.

## References

1. Elfring R, de la Fuente M, Radermacher K. Assessment of optical localizer accuracy for computer aided surgery systems. Comput Aided Surg. 2010; 15:1–12. [PubMed: 20233129]
2. Yaniv Z, Wilson E, Lindisch D, Cleary K. Electromagnetic tracking in the clinical environment. Med Phys. 2009; 36:876–892. [PubMed: 19378748]
3. Reichl T, Gardiazabal J, Navab N. Electromagnetic servoinga new tracking paradigm. IEEE Trans Med Imaging. 2013; 32:1526–1535. [PubMed: 23911947]

4. Bodner J, Wykypiel H, Wetscher G, Schmid T. First experiences with the da Vinci operating robot in thoracic surgery. Eur J Cardiothorac Surg. 2004; 25:844–851. [PubMed: 15082292]
5. Farivar AS, Cerfolio RJ, Vallieres E, Knight AW, Bryant A, Lingala V, Aye RW, Louie BE. Comparing robotic lung resection with thoracotomy and video-assisted thoracoscopic surgery cases entered into the society of thoracic surgeons database. Innovations (Phila). 2014; 9:10–15. [PubMed: 24553055]
6. Kent M, Wang T, Whyte R, Curran T, Flores R, Gangadharan S. Open, video-assisted thoracic surgery, and robotic lobectomy: review of a national database. Ann Thorac Surg. 2014; 97:236–244. [PubMed: 24090577]
7. Park BJ. Robotic lobectomy for non-small cell lung cancer (NSCLC): multi-center registry study of long-term oncologic results. Ann Cardiothorac Surg. 2012; 1:24–26. [PubMed: 23977460]
8. Pardolesi A, Park B, Petrella F, Borri A, Gasparri R, Veronesi G. Robotic anatomic segmentectomy of the lung: technical aspects and initial results. Ann Thorac Surg. 2012; 94:929–934. [PubMed: 22748642]
9. Kwoh YS, Hou J, Jonckheere EA, Hayati S. A robot with improved absolute positioning accuracy for CT guided stereotactic brain surgery. IEEE Trans Biomed Eng. 1988; 35:153–160. [PubMed: 3280462]
10. Schouten R, Lee R, Boyd M, Paquette S, Dvorak M, Kwon BK, Fisher C, Street J. Intra-operative cone-beam CT (O-arm) and stereotactic navigation in acute spinal trauma surgery. J Clin Neurosci Off J Neurosurg Soc Australas. 2012; 19:1137–1143.
11. Jin J-Y, Ryu S, Faber K, Mikkelsen T, Chen Q, Li S, Movsas B. 2D/3D Image fusion for accurate target localization and evaluation of a mask based stereotactic system in fractionated stereotactic radiotherapy of cranial lesions. Med Phys. 2006; 33:4557– 4566. [PubMed: 17278807]
12. Schmidt ML, Poulsen PR, Toftegaard J, Hoffmann L, Hansen D, Sorensen TS. Clinical use of iterative 4D-cone beam computed tomography reconstructions to investigate respiratory tumor motion in lung cancer patients. Acta Oncol. 2014; 53(8):1107–1113. [PubMed: 24957556]
13. Li R, Lewis JH, Jia X, Gu X, Folkerts M, Men C, Song WY, Jiang SB. 3D tumor localization through real-time volumetric xray imaging for lung cancer radiotherapy. Med Phys. 2011; 38:2783–2794. [PubMed: 21776815]
14. Awad J, Owrangi A, Villemaire L, O'Riordan E, Parraga G, Fenster A. Three-dimensional lung tumor segmentation from x-ray computed tomography using sparse field active models. Med Phys. 2012; 39:851–865. [PubMed: 22320795]
15. Li R, Jia X, Lewis JH, Gu X, Folkerts M, Men C, Jiang SB. Real-time volumetric image reconstruction and 3D tumor localization based on a single x-ray projection image for lung cancer radiotherapy. Med Phys. 2010; 37:2822–2826. [PubMed: 20632593]
16. Pan T, Riegel AC, Ahmad MU, Sun X, Chang JY, Luo D. New weighted maximum-intensity-projection images from cine CT for delineation of the lung tumor plus motion. Med Phys. 2013; 40:061901. [PubMed: 23718592]
17. Chen M, Bai J, Zheng Y, Siochi RA. 3D lung tumor motion model extraction from 2D projection images of mega-voltage cone beam CT via optimal graph search. Med Image Comput Comput Assist Interv. 2012; 15:239–246. [PubMed: 23285557]
18. Yang Y, Zhong Z, Guo X, Wang J, Anderson J, Solberg T, Mao W. A novel markerless technique to evaluate daily lung tumor motion based on conventional cone-beam CT projection data. Int J Radiat Oncol Biol Phys. 2012; 82:e749–e756. [PubMed: 22330989]
19. Mori S, Kanematsu N, Asakura H, Endo M. Projection-data based temporal maximum attenuation computed tomography: determination of internal target volume for lung cancer against intra-fraction motion. Phys Med Biol. 2007; 52:1027–1038. [PubMed: 17264368]
20. Brost, A.; Strobel, N.; Yatziv, L.; Gilson, WD.; Meyer, BC.; Hornegger, J.; Lewin, JS.; Wacker, FK. Geometric accuracy of 3-D X-ray image-based localization from two C-arm views. Workshop on geometric accuracy in image guided interventions—medical image computing and computer assisted interventions (MICCAI); London, UK. 2009.
21. Brost A, Strobel N, Yatziv L, Gilson WD, Meyer BC, Hornegger J, Lewin JS, Wacker FK. Accuracy of X-ray image-based 3D localization from two C-arm views: a comparison between an ideal system and a real device. SPIE medical imaging. 2009

22. Siemens' Artis zeego brings surgery and industry together. Cardiovasc J Afr. 2009; 20:258. [PubMed: 19701540]
23. Ma C, Hou Y, Li H, Li D, Zhang Y, Chen S, Yin Y. A study of the anatomic changes and dosimetric consequences in adaptive CRT of non-small-cell lung cancer using deformable CT and CBCT image registration. Technol Cancer Res Treat. 2014; 13:95–100. [PubMed: 23919391]
24. Pertl L, Gashi-Cenkoglu B, Reichmann J, Jakse N, Pertl C. Preoperative assessment of the mandibular canal in implant surgery: comparison of rotational panoramic radiography (OPG), computed tomography (CT) and cone beam computed tomography (CBCT) for preoperative assessment in implant surgery. Eur J Oral Implantol. 2013; 6:73–80. [PubMed: 23513204]
25. Angelopoulos C, Scarfe WC, Farman AG. A comparison of maxillofacial CBCT and medical CT. Atlas Oral Maxillofac Surg Clin N Am. 2012; 20:1–17.
26. Otake Y, Armand M, Armiger RS, Kutzer MD, Basafa E, Kazanzides P, Taylor RH. Intraoperative image-based multiview 2D/3D registration for image-guided orthopaedic surgery: incorporation of fiducial-based C-arm tracking and GPU-acceleration. IEEE Trans Med Imaging. 2012; 31:948–962. [PubMed: 22113773]
27. Pluim JP, Maintz JB, Viergever MA. Image registration by maximization of combined mutual information and gradient information. IEEE Trans Med Imaging. 2000; 19:809–814. [PubMed: 11055805]
28. Otake Y, Wang AS, Webster Stayman J, Uneri A, Kleinszig G, Vogt S, Khanna AJ, Gokaslan ZL, Siewerdsen JH. Robust 3D–2D image registration: application to spine interventions and vertebral labeling in the presence of anatomical deformation. Phys Med Biol. 2013; 58:8535–8553. [PubMed: 24246386]
29. Fitzpatrick JM, West JB, Maurer CR Jr. Predicting error in rigid-body point-based registration. IEEE Trans Med Imaging. 1998; 17:694–702. [PubMed: 9874293]
30. Otake Y, Schafer S, Stayman JW, Zbijewski W, Kleinszig G, Graumann R, Khanna AJ, Siewerdsen JH. Automatic localization of target vertebrae in spine surgery using fast CT-to-fluoroscopy (3D–2D) image registration. SPIE Medical Imaging 2012: Image-Guided Procedures, Robotic Interventions, and Modeling. 2012; 8316:8316N–8310N.
31. Uneri A, Otake Y, Wang AS, Kleinszig G, Vogt S, Khanna AJ, Siewerdsen JH. 3D–2D registration for surgical guidance: effect of projection view angles on registration accuracy. PhysMed Biol. 2013; 59:271–287.
32. Jain A, Kon R, Zhou Y, Fichtinger G. C-arm calibrationis it really necessary? Med Image Comput Comput Assist Interv. 2005; 8:639–646. [PubMed: 16685900]
33. Chintalapani G, Jain A, Taylor RH. Statistical characterization of C-arm distortion with application to intra-operative distortion correction. SPIE Medical Imaging 2007: Image-Guided Procedures, Robotic Interventions, and Modeling. 2007

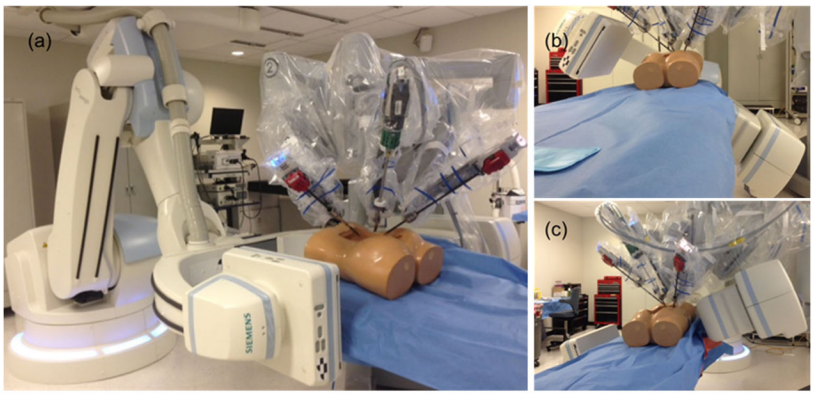


**Fig. 1.**

Photographs of the *da Vinci*-zeego workspace configuration experiment. **a** Zeego positioned at table head with docked patient-side-cart. C-arm of the zeego at the start (**b**) and **c** end of a ~45° scan range

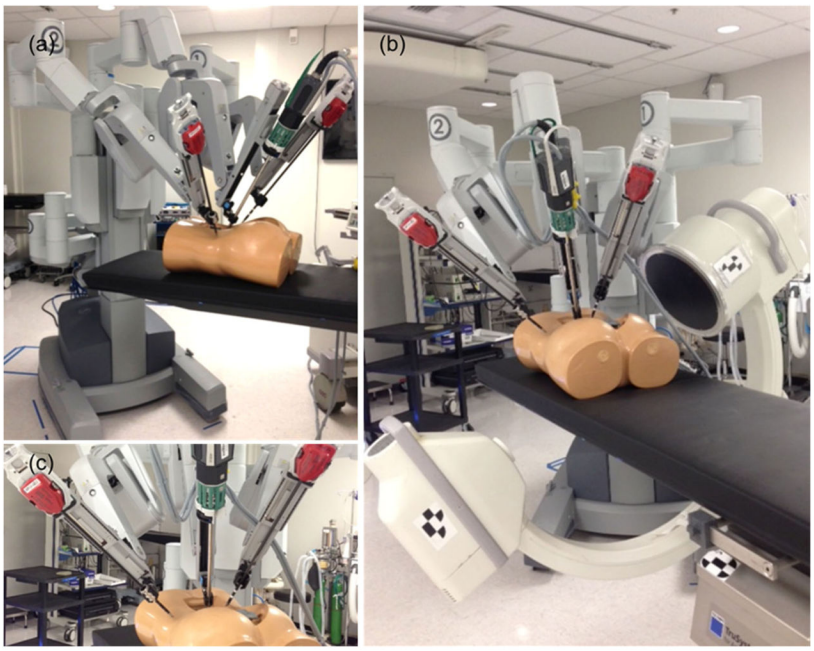


**Fig. 2.**

Photographs of the *da Vinci*-OEC workspace configuration (**a**). Position of PSC at ~30° to table (**b**). OEC 9600 at end of scan limit (30°) (**c**). Placement of *da Vinci* robotic arms for thoracic intervention

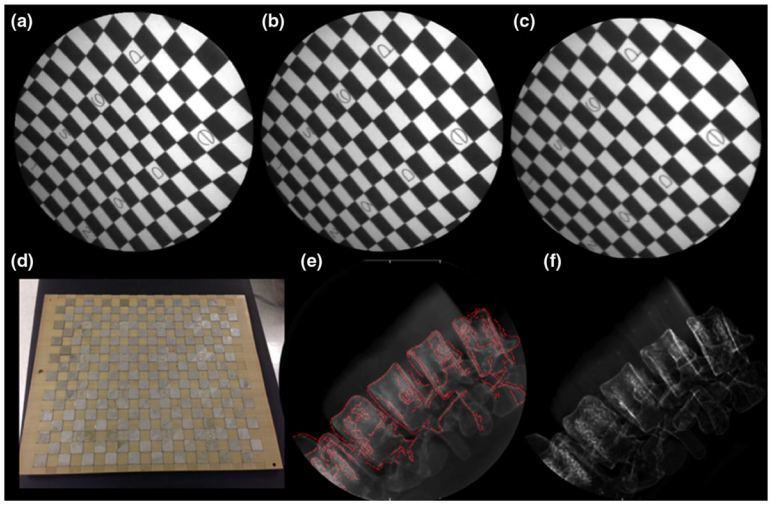


**Fig. 3.**

**a** Raw X-ray, **b** X-ray after radial and tangential rectification, **c** X-ray after (**b**) and S-distortion correction, **d** photograph of fluoroscopic checkerboard used for C-arm calibration. **e** Rectified OEC 9600 radiograph of Superflab-spine phantom with gradient (*red*) of registered DRR and **f** DRR generated during the 2D–3D registration

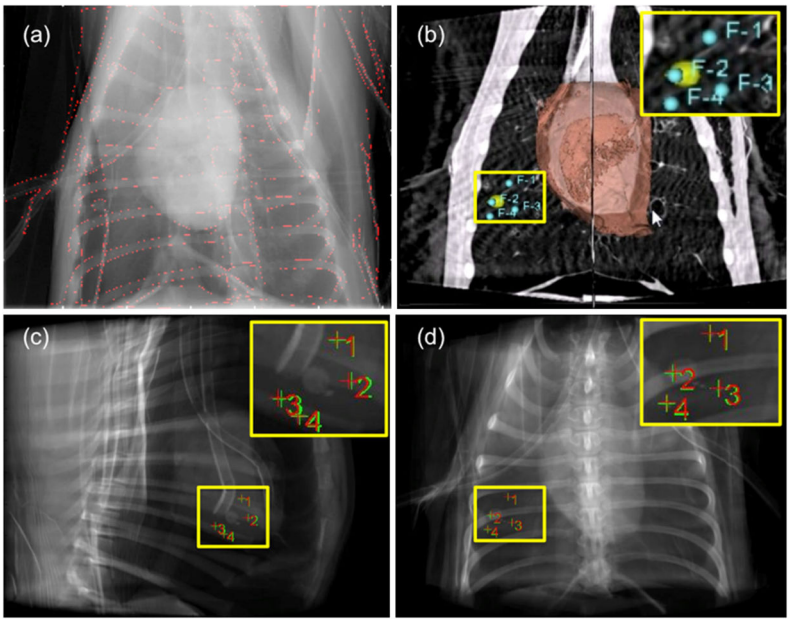


**Fig. 4.**

Radiographs during 2D–3D registration and DRR for ground truth assessment. **a** Anterior–posterior radiograph with gradient (*red*) of registered DRR. **b** Single coronal slice of reconstructed canine thorax with segmented heart (*orange*), mock tumor (*yellow*) and numbered peri-tumor fiducials (*blue*). **c** Sagittal and **d** coronal fluoroscopic image with forward projections of segmented 3D targets

| Perturb | ΔT = 10 ΔR = 1 | | n=100 |
|---|---|---|---|
| *Angle* | $TRE_{mean}$ | $TRE_{median}$ | $TRE_{max}$ |
| 15 | 41.8 | 41.7 | 43.1 |
| 30 | 12.7 | 12.6 | 13.3 |
| 45 | 5.0 | 5.1 | 5.2 |

| DRR | ΔT = 10 ΔR = 1 | | n=100 |
|---|---|---|---|
| *Angle* | $TRE_{mean}$ | $TRE_{median}$ | $TRE_{max}$ |
| 15 | 0.1 | 0.1 | 0.4 |
| 30 | 0.1 | 0.1 | 0.2 |
| 45 | 0.0 | 0.0 | 0.1 |

| Fluoro | ΔT = 10 ΔRz = 1 | | n=100 |
|---|---|---|---|
| *Angle* | $TRE_{mean}$ | $TRE_{median}$ | $TRE_{max}$ |
| 15 | 3.1 | 3.1 | 3.4 |
| 30 | 2.0 | 2.0 | 2.2 |
| 45 | 2.0 | 2.0 | 2.2 |

**TRE [mm]*

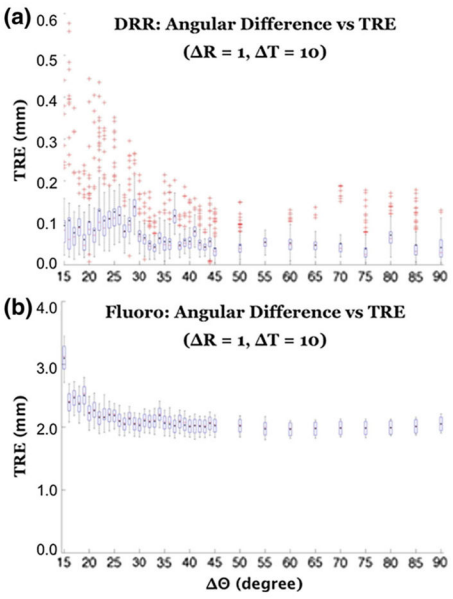


**Fig. 5.**

Results from dual projection experiments focused on Artis zeego extrinsic uncertainties. Table (*left*, *top*) TRE from perturbing fluroscopic data. Table (*left*, *medial*) TRE after 2D–3D registration on perturbed DRR data. Table (*left*, *bottom*) TRE after 2D–3D registration on perturbed fluoroscopic data. **a** *Box plot* of the zeego extrinsic uncertainty on after 2D–3D registration on DRR TRE (experiment #4). **b** *Box plot* of the zeego extrinsic uncertainty after 2D–3D registration on fluoroscopic TRE (experiment #3)

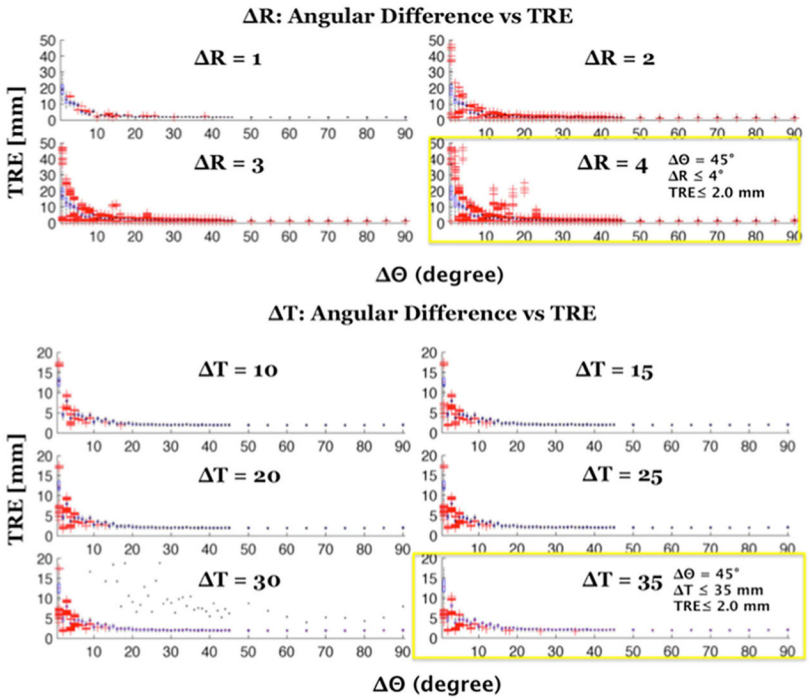


**Fig. 6.**

For Artis zeego: (*top* experiment #5) *box plot* of the effect of angular difference on TRE with various rotational perturbations. (*Bottom* experiment #6) *boxplot* of the effect of angular difference on TRE with various translational perturbations

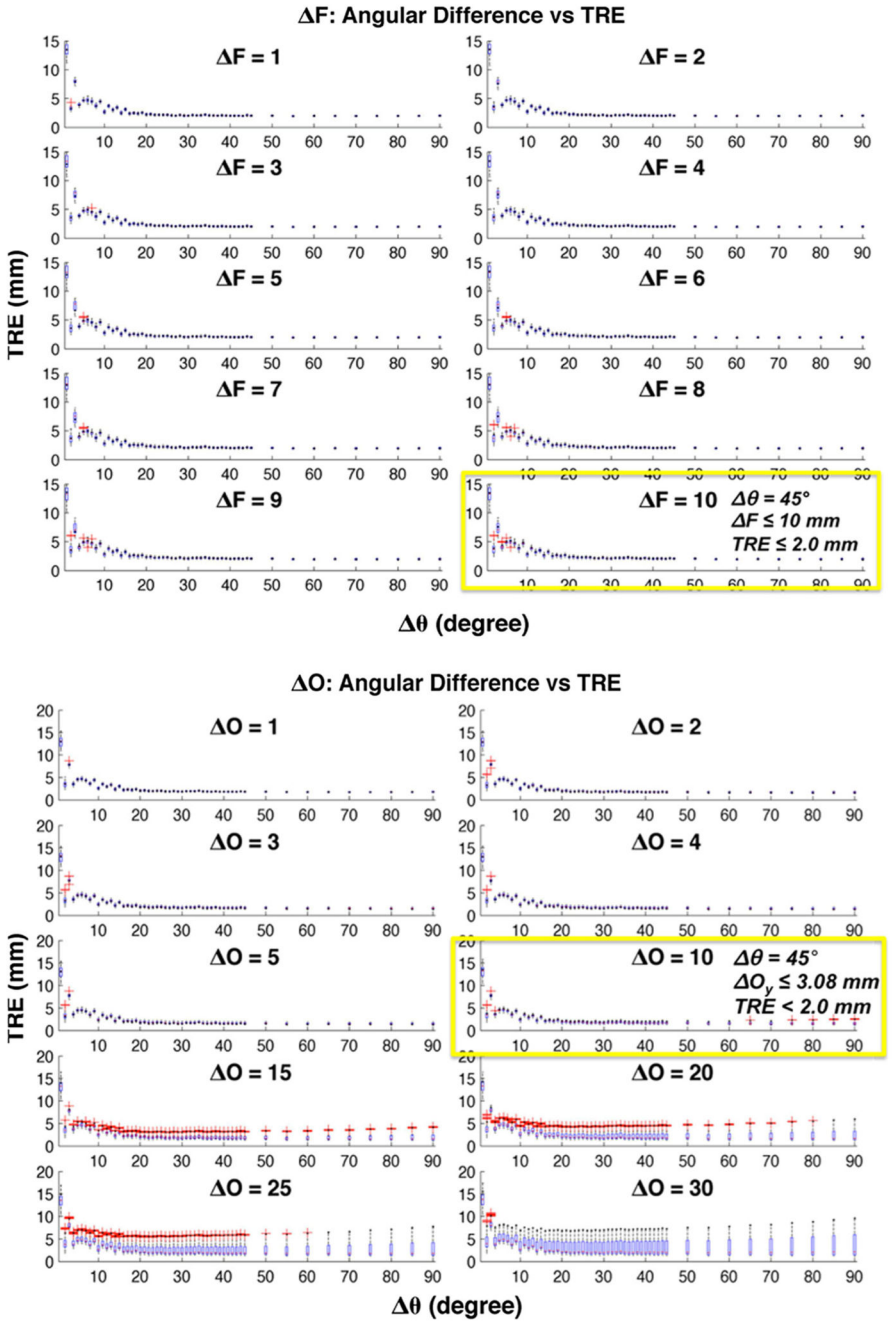


**Fig. 7.**

Zeego: (*top* experiment #7) *boxplot* of the effect of angular difference on TRE with various focal length perturbations. (*Bottom* experiment #8) *boxplot* of the effect of angular difference on TRE with various optical center perturbations

## Table 1

Preoperative and intraoperative workflow for proposed C-arm-guided wedge resection

| Step | Standard | OEC 9600 | Zeego |
|---|---|---|---|
| | | **Description** | **Description** |
| 1 | (Case Dep) | Biopsy | Biopsy |
| 2 | No | Place peritumor fiducial during biopsy | Place peritumor fiducial during biopsy |
| 3 | Yes | Obtain preoperative CT (supine, inflated) | Obtain preoperative CT (supine, inflated) |
| 4 | No[+] | Set up micron tracker | Obtain intraoperative CBCT (supine, inflated) |
| | No[+] | | Use iGuide to place 1 or more fiducials near target |
| 5 | Yes | Rotate patient to lateral and collapse lung | Rotate patient to lateral and collapse lung |
| 6 | No | Register preop CT | Obtain intraoperative CBCT (lateral, inflated) |
| 7 | Yes | Place trocars and set up da Vinci (Fig. 2a, c) | Place trocars and set up da Vinci (Fig. 2a, c) |
| 8 | No | Set up C-arm to image patient from posterior to anterior | Set up C-arm to image patient from posterior to anterior |
| 9 | No | Acquire dual X-rays to locate (3D) radio-opaque points of interest[*] | Acquire dual X-rays to locate (3D) radio-opaque points of interest[*] |

[+] Optional if Step 2 performed

[*] Repeat as needed for intraoperative confirmation

**Table 2**

2D–3D registration and optimization parameters with nominal values

| System | Component | Parameter | Nominal value | |
|---|---|---|---|---|
| OEC 9600 | Initialization | Perturbation | (Table 3) | – |
| | Optimizer | Population size | 50–100 | – |
| | | Step size | 5 | (mm,° ) |
| | | Lower/upper bounds | ±10 | (mm,° ) |
| | | Stopping criterion | 0.01 | (mm,° ) |
| | C-arm | SID | 680 | (mm) |
| | | SDD | 980 | (mm) |
| | CBCT | Voxel size | 0.48 | (mm) |
| | Fluoro | Pixel size | 0.45 | (mm) |
| | Image selection | Angular disparity | 30 | (°) |
| Zeego | Initialization | Perturbation | (Table 3) | – |
| | Optimizer | Population size | 50–100 | – |
| | | Step size | 5 | (mm,° ) |
| | | Lower/upper bounds | ±10 | (mm,° ) |
| | | Stopping criterion | 0.01 | (mm,° ) |
| | C-arm | SID | 785 | (mm) |
| | | SDD | 1,200 | (mm) |
| | CBCT | Voxel size | 0.48 | (mm) |
| | Fluoro | Pixel size | 0.308 | (mm) |
| | Image selection | Angular disparity | 0–90 | (°) |

**Table 3**

Variation of angular difference ($\Delta\theta$), extrinsic ($\Delta R$, $\Delta T$ ) and intrinsic ($\Delta F$, $\Delta O$) uncertainty in 2D–3D image registration experiments

| Exp # | C-arm system | Image | Phantom | $\Delta\Theta$ (°) | $\Delta F$ (mm) | $\Delta O$ (pix) | $\Delta R$ (°) | $\Delta T$ (mm) |
|---|---|---|---|---|---|---|---|---|
| 1 | OEC 9600 | Radiograph | Superflab + Spine | 30 | 0 | 0 | 3 | 10 |
| 2 | OEC 9600 w/tracker | Radiograph | Superflab + Spine | 30 | 0 | 0 | 1 | 2 |
| 3 | Zeego | Radiograph | Canine | 1–90 | 0 | 0 | 1 | 1–10 |
| 4 | Zeego | DRR | Canine | 1–90 | 0 | 0 | 1 | 1–10 |
| 5 | Zeego | Radiograph | Canine | 1–90 | 0 | 0 | 1–10 | 0 |
| 6 | Zeego | Radiograph | Canine | 1–90 | 0 | 0 | 0 | 5–50 |
| 7 | Zeego | Radiograph | Canine | 1–90 | 1–10 | 0 | 0 | 0 |
| 8 | Zeego | Radiograph | Canine | 1–90 | 0 | 1–30 | 0 | 0 |

*Int J Comput Assist Radiol Surg*. Author manuscript; available in PMC 2015 August 05.

**Table 4**

OEC 9600: 2D–3D TRE from experiments with variable rectification and extrinsic ($\Delta R$, $\Delta T$ ) uncertainty

| Rectification | $TRE_{mean}$ | $TRE_{median}$ | $TRE_{max}$ | *p* value |
|---|---|---|---|---|
| OEC | $\Delta\theta$ = 30ΔR = 3°ΔT = 0 mm *n* = 100 | | | |
| None | 43.4 | 43.5 | 60.9 | Ref |
| Radial, tangential | 37.2 | 37.6 | 41.6 | 0.0010 |
| S, radial, tangential | 8.7 | 8.8 | 18.7 | 0.0004 |
| OEC | $\Delta\theta$ = 30ΔR = 0° ΔT = 10 mm *n* = 100 | | | |
| None | 27.7 | 27.5 | 31.2 | Ref |
| Radial, tangential | 4.8 | 4.8 | 6.2 | 0.0030 |
| S, radial, tangential | 3.7 | 3.7 | 6.9 | 0.0020 |
| OEC w/tracker | $\Delta\theta$ = 30ΔR = 3° ΔT = 10 mm *n* = 100 | | | |
| None | 46.0 | 46.0 | 56.4 | ref |
| Radial, tangential | 44.7 | 45.2 | 46.7 | 0.0200 |
| S, radial, tangential | 9.6 | 9.7 | 17.8 | 0.0100 |
| OEC w/tracker | $\Delta\theta$ = 30ΔR = 1° ΔT = 10 mm *n* = 100 | | | |
| None | 29.2 | 29.2 | 36.1 | Ref |
| Radial, tangential | 25.3 | 25.6 | 32.7 | 0.0011 |
| S, radial, tangential | 2.5 | 2.5 | 7.1 | 0.0005 |
| OEC w/tracker | $\Delta\theta$ = 30ΔR = 0° ΔT = 2 mm *n* = 100 | | | |
| None | 21.8 | 21.6 | 24.1 | Ref |
| Radial, tangential | 3.6 | 3.5 | 4.5 | 0.0110 |
| S, radial, tangential | 2.1 | 2.0 | 4.2 | 0.0100 |
| OEC w/tracker | $\Delta\theta$ = 30ΔR = 1° ΔT = 2 mm *n* = 100 | | | |
| None | 31.1 | 31.0 | 34.9 | Ref |
| Radial, tangential | 26.8 | 27.1 | 34.0 | 0.0200 |
| S, radial, tangential | 2.4 | 2.5 | 9.8 | 0.0100 |